Advances in Differential Equations and Control Processes 2026, 33(3), 4582.
doi: https://doi.org/10.59400/adecp4582

Article

GRF-based trajectory planning and application for bipedal motion

Qianying Zhu[1], Aliyu Hamza[1], Yanan Gao[1,*], Jiaqi Gao[2], Shouhua Liu[1], Enping Guo[3], Qiuyue Cheng[4], Yanxiang Chen[3], Yuanyang Chen[1], Yue Wang[5]

[1] Faculty of Architecture and Civil Engineering, Huai'an University, Huai'an 223001, China; zqy12180043@hyit.edu.cn (QZ); S257808008@hyit.edu.cn (AH); liushouhua@hau.edu.cn (SL); chen.yuanyang@qq.com (YC)

[2] College of Traditional Chinese Medicine, Xinjiang Medical University, Urumqi 830011, China; gaojiaqi669@sina.com

[3] School of Civil and Environmental Engineering, Hunan Institute of Science and Engineering, Yongzhou 425199, China; guoenping@huse.edu.cn (EG); chenyanxiang2377@huse.edu.cn (YC)

[4] School of Architectural Engineering, Chuzhou Polytechnic College, Chuzhou 239000, China; chengqiuyue@chzc.edu.cn

[5] Jiangsu Huaiyin Power Generation Co., Ltd., Huai'an 223002, China; elainewong0426@hotmail.com

* **Corresponding authors:** Yanan Gao, gaoyn@hau.edu.cn

CITATION

Zhu Q, Hamza A, Gao Y, et al. GRF-based trajectory planning and application for bipedal motion. Advances in Differential Equations and Control Processes. 2026; 33(3): 4582. https://doi.org/10.59400/adecp4582

ARTICLE INFO

Received: 29 July 2026
Revised: 15 August 2026
Accepted: 20 August 2026
Available online: 26 August 2026

Abstract: Trajectory planning for the center of mass (CoM) constitutes a fundamental challenge in bipedal locomotion. Conventional approaches, which predominantly rely on experimental measurements or simplified analytical models, are often constrained by discretization errors, parameter uncertainty, and prohibitive experimental costs. To address these limitations, this paper proposes a numerical framework for generating CoM trajectories directly from ground reaction force (GRF) dynamics. The methodology first determines key gait event positions and formulates a coupled system of governing equations that integrate force and motion. The method then establishes a unified spatio-temporal-GRF coordinate system and incorporates boundary conditions, along with load-sharing mechanisms between the trailing and leading legs, to derive the force and geometric constraint equations. The resulting reference trajectory is represented using Fourier coefficients, which are determined via an Adam-based constrained residual minimization solver. This Fourier-based representation offers notable advantages, including a compact parameter set, high computational efficiency, and the capacity to capture the essential kinematic features of bipedal walking. To validate the proposed reference trajectory, a sliding mode control (SMC) framework is employed for bipedal walking control, in which the walker successfully tracks the reference trajectory with stable gait execution. The results confirm that the generated trajectory faithfully reproduces the characteristic CoM response of bipedal walking, thereby providing a high-fidelity reference for robust motion control. Furthermore, a systematic analysis of the control parameters is conducted to evaluate their influence on walking stability. This work offers a new paradigm that synergistically combines physical interpretability with computational efficiency, holding significant promise for applications in humanoid robot motion control and biomechanical analysis.

Keywords: bipedal gait; ground reaction force; trajectory design; sliding mode control; application verification

1. Introduction

Bipedal dynamic walking stands as one of the most persistent grand challenges in robotics, driven by the ambition to replicate the efficiency and adaptability of human locomotion. At the heart of this problem lies the planning and control of the robot's center of mass (CoM). As the principal variable encapsulating whole-body dynamics, CoM trajectory directly shapes gait stability, energetic cost, and the capacity to handle uneven terrain. In both human and robotic walking, CoM traces a three-dimensional cyclic path whose regularity and shape serve as a direct window into balance performance and locomotor maturity [1]. It is no surprise, then, that a large body of work has sought to develop tractable yet physically grounded methods for constructing CoM reference trajectories that steer the system through alternating single- and double-support phases.

The traditional starting point for CoM trajectory planning has been the use of drastically simplified dynamic models. Among them, the Linear Inverted Pendulum (LIP) [2, 3] and the associated Zero Moment Point (ZMP) criterion [4] form the most established framework. The LIP reduces the multibody dynamics of a walking machine to a point mass gliding at a fixed height above a compliant pivot, while the ZMP constraint demands that the instantaneous point of zero net moment stays within the support polygon, thereby ensuring dynamic balance. Together, these simplifications collapse the planning problem into one that admits closed-form or low-order numerical solutions, a property that has been exploited on numerous humanoid platforms. Extensions of this idea have used numerical regression with the LIP to prescribe both the walking direction and the vertical motion of CoM [5], widening the practical scope of the approach.

Yet the simplifications that make the LIP attractive are also its most severe liability. Constant CoM height, vanishing angular momentum about CoM, and massless legs combine to impose hard bounds on achievable dynamic performance [6]. The resulting gaits tend to be conservative and quasi-static, appearing stiff and mechanical next to biological walking. Energy efficiency suffers as well: fixing CoM height eliminates the vertical oscillation that underpins the inverted-pendulum energy-exchange mechanism observed in natural gait [7]. Higher-order variants—the Variable-Height Inverted Pendulum, the Reaction Mass Pendulum—relax some of these constraints by allowing vertical CoM motion or capturing torso rotational inertia [8,9], but they inevitably trade away the analytical simplicity of the original LIP, pushing the problem back toward heavy numerical computation.

In response to these limits, Model Predictive Control (MPC) has gained considerable traction for centroidal trajectory generation over the past decade [10]. MPC recasts planning as a finite-horizon optimal control problem that is resolved at each control cycle, delivering CoM trajectories that satisfy dynamic constraints through online rolling optimization [11]. By folding in inequality constraints, contact schedules, and user-defined cost terms, MPC markedly bolsters robustness, particularly against external disturbances and model mismatch [12]. Still, the computational load of iterative online optimization is substantial, and the solutions remain acutely sensitive to the choice of prediction horizon, cost weights, and terminal constraints—tuning challenges that can hinder real-time deployment on physical robots.

At a deeper level, the prevailing planning paradigms—whether offline methods rooted in simple models or online schemes based on MPC—share a fundamental conceptual gap: none of them establish an explicit, analytical link between CoM motion and the ground reaction force (GRF). The GRF is the only external agent that accelerates and decelerates a legged system during stance; its temporal profile captures the essence of dynamic walking—the characteristic double-peaked vertical force, the smooth transfer of load from the trailing limb to the leading limb, and the transient unloading around mid-stance [13,14]. Yet mainstream approaches treat CoM trajectory generation and GRF allocation as largely separate subproblems[15,16], connected only through numerical integration and time parameterization. This decoupling lets integration errors accumulate, so that planned trajectories drift away from physically admissible solutions over long walking sequences. It also severs the conceptual connection between CoM's dynamic behavior and the discrete gait-phase structure of bipedal locomotion, making it exceedingly difficult to reproduce the subtle interplay of force buildup, transfer, and release that characterizes efficient alternating support [17, 18]. Experimental work reinforces this picture: during single support, ground reaction forces are directed toward a virtual pivot point located above CoM, whereas during double support they converge around CoM itself, with markedly different horizontal-to-vertical force ratios [19]. A planning framework that ignores these phase-dependent force characteristics necessarily trades physical fidelity for convenience.

The present study introduces a different strategy—a numerical paradigm for CoM trajectory generation that is built directly from ground reaction force dynamics. The contribution is a method that produces dual-footed walking centroid reference trajectories without recourse to iterative numerical integration or online optimization. A unified mathematical framework is established that simultaneously encodes the temporal, spatial, and GRF dimensions of bipedal walking, and the CoM path—most notably its vertical trajectory, which has historically been the most resistant to accurate planning—is derived analytically from GRF constraints [20]. Continuous weighting functions coordinate the path allocation between the trailing and leading legs throughout the support phase, yielding smooth, continuous, and physically consistent CoM trajectories that respect the underlying force profile at every instant [21–23]. The resulting planner inherently captures the dynamic switching structure of bipedal alternating support, producing natural gaits with clean force transfer, low jerk—qualities that have remained elusive under purely model-driven or purely optimization-driven formulations [24,25].

2. Parameter analysis

The ground reaction force in bipedal walking traces out a characteristic two-peak pattern over the stance phase [26]. **Figure 1** displays the complete GRF profiles of the leading foot (F_l) and the trailing foot (F_τ) from touchdown to toe-off plotted against time t.

The duration of the stance phase of a single foot from touchdown to toe-off is defined as T_e, the time offset between the touchdowns of the two feet is defined as T_s, and the time interval from touchdown to the valley of the GRF is defined as T_v. Taking the instant of the GRF valley (at time T_v after touchdown of the trailing foot) as the time origin, a coordinate system t-o-z is established. In this coordinate system, z represents the vertical position of the CoM of the bipedal model, denoted by $z(t)$; $x(t)$ and $y(t)$ are the fore–aft and lateral displacements of CoM, respectively. The step length and step width are denoted by L_s and L_w. Within the *t*-*o*-*z* frame, the instant of leading-foot touchdown is labeled t_1 and the instant of trailing-foot toe-off is labeled t_2. At t_1, the distance from CoM to the trailing foot is D_1; at t_2, the distance from CoM to the leading foot is D_3. The angles between the trailing leg and the ground and between the leading leg and the ground are denoted by θ_τ and θ_ι, respectively, and k_{leg} is the leg stiffness. Damping is neglected in the present model, and it is further assumed that at the GRF valley instant T_v, the pedestrian is in an upright single-support stance phase. The single GRF $F(t)$ is expressed by the Fourier series given in Equation (1) [27,28] from 1.6 Hz to 2.4 Hz with walking frequency f_s, whose parameters are listed in **Table 1**.

$$F(T) = G\sum_{n=1}^{5} \phi_n sin\left(\frac{n\pi T}{T_e}\right) \quad T \in [0,\ T_e] \tag{1}$$

where G is the weight of human body and f_n is load factor.

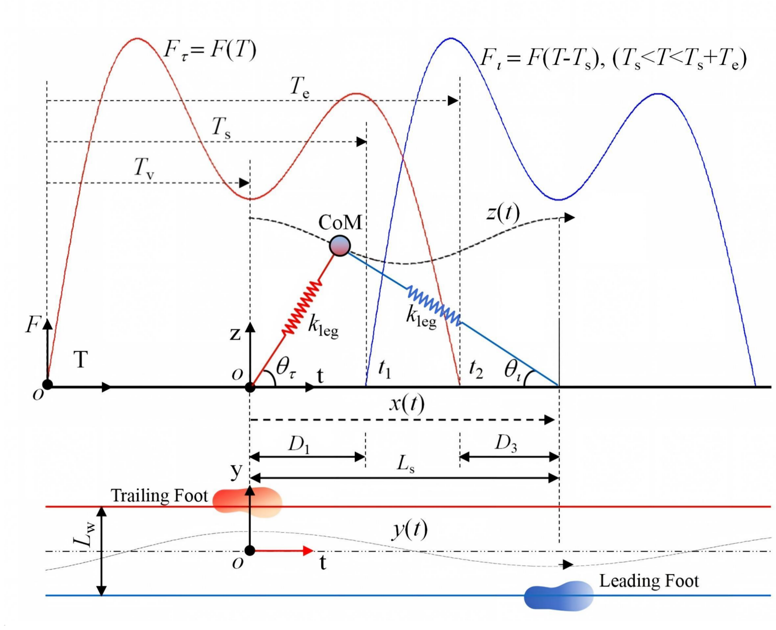

Figure 1. Spatiotemporal relationship between GRF and CoM trajectory.

Table 1. Load factors of GRF model [27].

	1.6 Hz $\leq f_s \leq$ 2.32 Hz	**2.32 Hz $< f_s \leq$ 2.4 Hz**
f_1	$-0.0698f_s + 1.211$	$-0.1784f_s + 1.463$
f_2	$0.1052f_s - 0.1284$	$-0.4716f_s + 1.210$
f_3	$0.3002f_s - 0.1534$	$-0.0118f_s + 0.5703$
f_4	$0.0416f_s - 0.0288$	$-0.2600f_s + 0.6711$
f_5	$-0.0275f_s + 0.0608$	$-0.0906f_s - 0.2132$

According to Fan et al. [27], the time difference $t_2 - t_1$ equals $0.24T_e$. To determine the parameter T_v that corresponds to the time instant of the valley position in the GRF curve, the GRF was examined over step frequencies ranging from 1.6 Hz to 2.4 Hz. Within each cycle, the minimum was located in the interval from 0.24 T_e to 0.76 T_e, and the time instant of this minimum was taken as T_v. The ratio T_v / T_e was then computed, as shown in **Figure 2**. The results reveal that for $f_s < 2.32$ Hz, T_v/T_e exhibits an exponential dependence on f_s. For $2.32 < f_s < 2.3634$ Hz, the ratio remains constant at 0.4991. In the rightmost frequency interval, i.e., from 2.3634 Hz to 2.42.4 Hz, T_v/T_e takes the value 0.4933. The overall relationship is described by Equation (2).

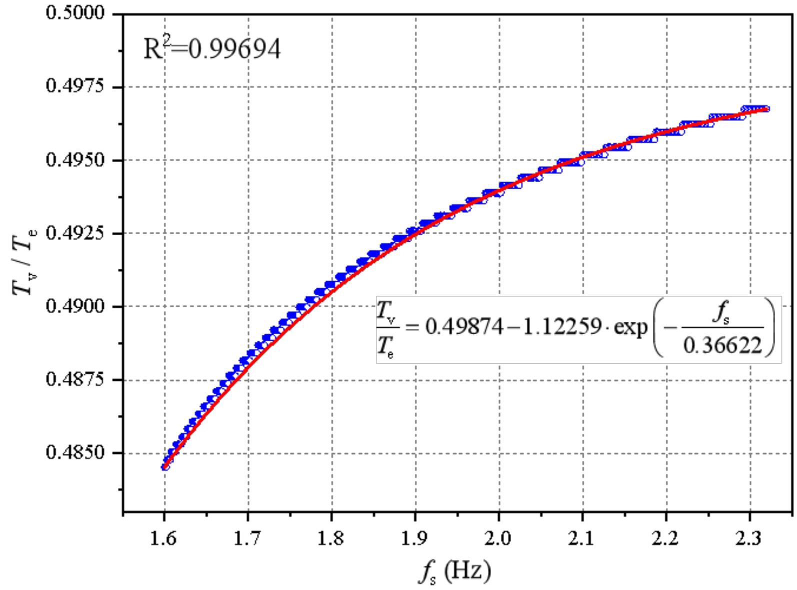

Figure 2. Fit between step frequency and T_v/T_e.

Note: The blue circles represent the discrete calculated values of T_v/T_e at different step frequencies, and the red curve represents the fitted curve of T_v/T_e.

$$\frac{T_v}{T_e} = \begin{cases} 0.49874 - 1.12259exp\left(-\frac{f_s}{0.36622}\right) & f_s \in [1.6 \text{ Hz},\ 2.32 \text{ Hz}] \\ 0.4991 & f_s \in \ 2.32 \text{ Hz}, 2.3634 \text{ Hz} \\ 0.4993 & f_s \in \ 2.3634 \text{ Hz}, 2.4 \text{ Hz} \end{cases} \tag{2}$$

After T_v is determined, according to the described procedure, $t_1 = T_s - T_v$ and $t_2 = T_e - T_v$ can be obtained, respectively. Under the previous assumption that the damping effect of the human leg on GRF is ignored, GRF can be expressed as:

$$F = k_{\text{leg}} (l_0 - l) \frac{z}{l} \tag{3}$$

where, z denotes CoM height, l_0 represents the natural leg length, l is the leg time-varying length under compression, and k_{leg} is the leg's equivalent stiffness coefficient. When CoM is at t_1, the leading foot is in a ground-free position with the leading leg at its natural length l_0.

The geometric analysis yields:

$$\begin{cases} \frac{k_{\text{leg}}[l_0 - l_\tau(t_1)]z(t_1)}{l_\tau(t_1)} = F_{\tau 1} \\ l_{\tau-yz}^2 + (L_s - D_1)^2 = l_0^2 \\ l_{\tau-yz}^2 + D_1^2 = l_\tau^2(t_1) \\ z^2(t_1) + \left[\frac{L_w}{2} - y(t_1)\right]^2 = l_{\tau-yz}^2 \end{cases} \tag{4}$$

where l_τ and $F_{\tau 1} = F_s(T_v + t_1)$ represent the lengths of the trailing leg and the GRF of the follower foot at time t_1, respectively. The above three sub-equations contain three unknown variables, namely D_1, $z(t_1)$, and $l_\tau(t_1)$. Eliminating $z(t_1)$ and $l_\tau(t_1)$ from the above Equation (4) yields the following polynomial in D_1:

$$4L_s^2D_1^6 - 20L_s^3D_1^5 + a_4D_1^4 + a_3D_1^3 + a_2D_1^2 + a_1D_1 + a_0 = 0 \tag{5}$$

The polynomial coefficients are as follows:

$$\begin{aligned} a_4 &= L_s^2\left(41L_s^2 - 8l_0^2 + 8\delta_{\tau1}^2\right) \\ a_3 &= 4L_s\left(6l_0^2L_s^2 - 6L_s^2\delta_{\tau1}^2 + 3l_0^2\delta_{\tau1}^2 - 11L_s^4\right) \\ a_2 &= 26L_s^4\left(L_s^2 - l_0^2 + \delta_{\tau1}^2\right) + 2L_s^2\left(2l_0^4 + 2\delta_{\tau1}^4 - 19l_0^2\delta_{\tau1}^2\right) + 4l_0^4\delta_{\tau1}^2 \\ a_1 &= 4L_s\left(l_0^2 - L_s^2\right)\left[L_s^2\left(2L_s^2 - l_0^2 + 3\delta_{\tau1}^2\right) + \delta_{\tau1}^2\left(\delta_{\tau1}^2 - 5l_0^2\right)\right] \\ a_0 &= \left(l_0^2 - L_s^2\right)^2\left(L_s^4 + 2L_s^2\delta_{\tau1}^2 - 4l_0^2\delta_{\tau1}^2 + \delta_{\tau1}^4\right) \end{aligned} \tag{6}$$

where $\delta_{\tau1} = \frac{F_{\tau1}}{k_{\text{leg}}}$ is the ratio of the ground reaction force F_τ of the trailing leg at time t_1 to the leg stiffness coefficient k_{leg}. Similarly, at time point t_2, the following leg has a length of l_0, and the following relational equation can be obtained:

$$\begin{cases} \frac{k_{\text{leg}}[l_0 - l_\iota(t_2)]z(t_2)}{l_\iota(t_2)} = F_{\iota2} \\ l_{\iota-yz}^2 + (L_s - D_3)^2 = l_0^2 \\ l_{\iota-yz}^2 + D_3^2 = l_\iota^2(t_3) \\ z^2(t_2) + \left[\frac{L_w}{2} + y(t_2)\right]^2 = l_{\iota-yz}^2 \end{cases} \tag{7}$$

where l_ι and $F_{\iota2} = F_s(T_s - t_1)$ represent the lengths of the leading leg and the GRF of the follower foot at time t_2, respectively. The above three sub-equations contain three unknown variables, namely D_3, $z(t_2)$, and $l_\iota(t_2)$. Eliminating $z(t_2)$ and $l_\iota(t_2)$ from the above Equation (7) yields the following polynomial in D_3:

$$4L_s^2D_3^6 - 20L_s^3D_3^5 + b_4D_3^4 + b_3D_3^3 + b_2D_3^2 + b_1D_3 + b_0 = 0 \tag{8}$$

The polynomial coefficients are also as follows:

$$\begin{aligned} b_4 &= L_s^2\left(41L_s^2 - 8l_0^2 + 8\delta_{\iota2}^2\right) \\ b_3 &= 4L_s\left(6l_0^2L_s^2 - 6L_s^2\delta_{\iota2}^2 + 3l_0^2\delta_{\iota2}^2 - 11L_s^4\right) \\ b_2 &= 26L_s^4\left(L_s^2 - l_0^2 + \delta_{\iota2}^2\right) + 2L_s^2\left(2l_0^4 + 2\delta_{\iota2}^4 - 19l_0^2\delta_{\iota2}^2\right) + 4l_0^4\delta_{\iota2}^2 \\ a_1 &= 4L_s\left(l_0^2 - L_s^2\right)\left[L_s^2\left(2L_s^2 - l_0^2 + 3\delta_{\iota2}^2\right) + \delta_{\iota2}^2\left(\delta_{\iota2}^2 - 5l_0^2\right)\right] \\ a_0 &= \left(l_0^2 - L_s^2\right)^2\left(L_s^4 + 2L_s^2\delta_{\iota2}^2 - 4l_0^2\delta_{\iota2}^2 + \delta_{\iota2}^4\right) \end{aligned} \tag{9}$$

where, $\delta_{\iota2} = \frac{F_{\iota2}}{k_{\text{leg}}}$ is the ratio of the ground reaction force F_ι of the trailing leg at time t_2 to the leg stiffness coefficient k_{leg}.

Equations (5) and (8) are sixth-order polynomial equations that have no analytical solution, but numerical roots can be obtained [28]. Among the six roots, only those that satisfy the following physical constraints are retained: the root must be a positive real number (negative and complex roots are discarded) and must be less than half the step length (i.e., $D_1, D_3 < 0.5L_s$). Applying these criteria eliminates the other five roots and yields a unique, physically admissible solution for D_1 and D_3. After filtering out the roots that do not meet the conditions, **Figure 3** presents the relationship curves between parameters D_1 and D_3 as a function of the step frequency (T_s/T_e) under different conditions. Analysis reveals that when the T_s/T_e ratio varies from 0.52 to 0.92, both D_1 and D_3 exhibit a nonlinear trend of first decreasing and then increasing. Specifically, in the lower ratio range ($T_s/T_e < 0.76$–0.8), increasing step frequency significantly raises the values of D_1 and D_3. At higher ratios ($T_s/T_e > 0.76$–0.8), however, raising the step frequency brings D_1 and D_3 down rather than up. Near $T_s/T_e = 0.67$, the two curves cross, after which changes in step frequency have little further effect on either parameter. What emerges is that CoM velocity distribution along the walking direction is far from uniform—it is shaped jointly by step frequency and the T_s/T_e ratio. **Figure 4** shows the values for step frequencies ranging from 1.6 to 2.4 Hz and step lengths ranging from 0.5 to 0.7 m.

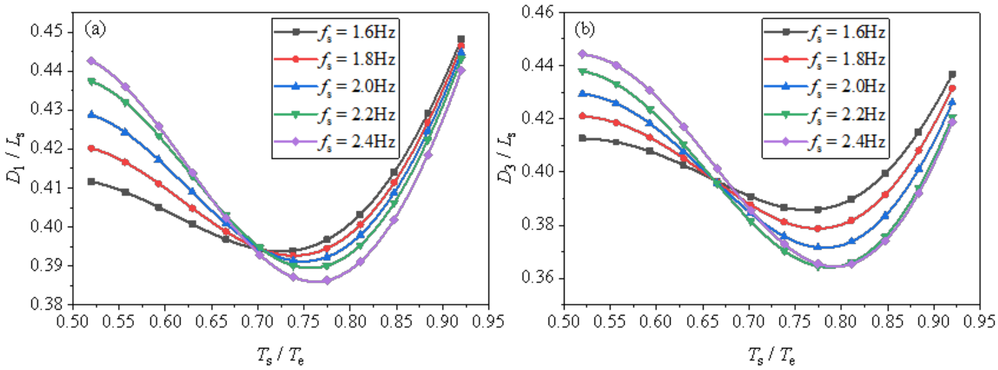

Figure 3. Variation curves of parameters D_1 and D_3 with T_s/T_e.

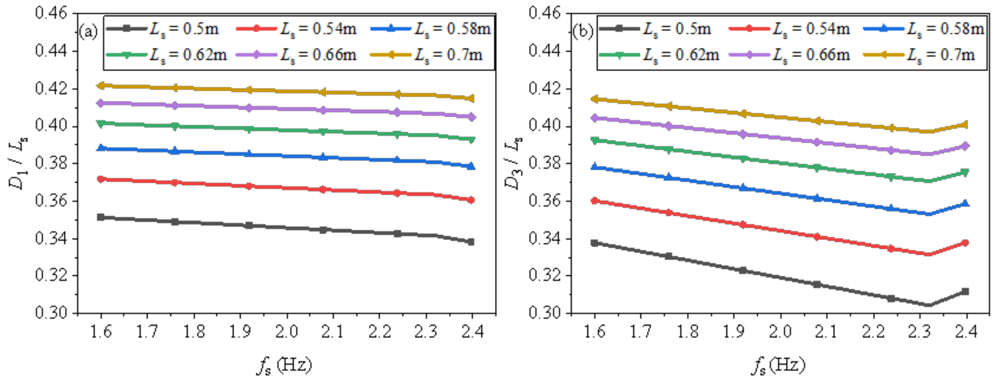

Figure 4. D_1 and D_3 with step frequency ($T_s/T_e = 0.76$).

It can be seen from the **Figure 4** that as the step frequency increases, both D_1/L_s and D_3/L_s generally exhibit a decreasing trend, with the exception that D_3/L_s increases after 2.32 Hz. This reversal is due to the change in the dynamic load factor at 2.32 Hz. When the step frequency exceeds 2.32 Hz, D_1/L_s decreases more rapidly while D_3/L_s rises more steeply as T_s/T_e increases. Physically, this indicates that at the instant of leading-foot touchdown, the distance between CoM and the trailing foot diminishes more quickly, whereas at the instant of trailing-foot liftoff, the distance from CoM to the leading foot becomes larger. This growing asymmetry between the two support phases implies that the body transfers onto the leading leg more abruptly and detaches from the trailing leg more rapidly, which introduces a potential bouncing effect and suggests a tendency for the gait to transition into running. Furthermore, the ratios of both D_1/L_s and D_3/L_s increase with step length. Thus, the values of D_1 and D_3 are influenced by both step frequency and GRF parameters.

3. Forward CoM trajectory

After obtaining the above parameters, it is established that $x(t)$ satisfies the four temporal boundary conditions: $x(0) = 0$, $x(t_1) = D_1$, $x(t_2) = L_s - D_3$, and $x(T_s) = L_s$. Furthermore, $x(t)$ must be a monotonically increasing function. This requirement arises from the fundamental characteristic of bipedal walking: CoM continuously moves forward throughout the gait cycle and never reverses direction between successive footfalls. Ensuring monotonicity is therefore essential for generating a physically realistic and controllable reference trajectory [29–31]. In addition, $x(t)$ is smooth and differentiable, and its first and second derivatives at $t = 0$ are equal to those at $t = T_s$, guaranteeing continuity and smoothness of the velocity and acceleration profiles across consecutive steps. Based on these conditions, a Fourier series representation is adopted, and the following expression for $x(t)$ is constructed to satisfy all the imposed boundary and continuity constraints:

$$x(t) = L_s f_s t + \alpha_x sin\left(2\pi f_s t\right) + \beta_x\left[cos\left(2\pi f_s t\right) - 1\right] \tag{10}$$

The above equation already inherently satisfies the conditions $x(0) = 0$, $x(T_s) = L_s$, and that its first and second derivatives at $t = 0$ are equal to those at $t = T_s$. Therefore, substituting it into the remaining two constraints $x(t_1) = D_1$ and $x(t_2) = L_s - D_3$ yields:

$$\begin{cases} \alpha_x sin\left(2\pi f_s t_1\right) + \beta_x\left[cos\left(2\pi f_s t_1\right) - 1\right] = D_1 - L_s f_s t_1 \\ \alpha_x sin\left(2\pi f_s t_2\right) + \beta_x\left[cos\left(2\pi f_s t_2\right) - 1\right] = L_s - D_3 - L_s f_s t_2 \end{cases} \tag{11}$$

Solving the above equations yields the following coefficient solutions:

$$\begin{cases} \alpha_x = \frac{[cos(2\pi f_s t_1) - 1](L_s - D_3 - L_s f_s t_2) - [cos(2\pi f_s t_2) - 1](D_1 - L_s f_s t_1)}{[cos(2\pi f_s t_1) - 1]sin(2\pi f_s t_2) - [cos(2\pi f_s t_2) - 1]sin(2\pi f_s t_1)} \\ \beta_x = \frac{(D_1 - L_s f_s t_1)sin(2\pi f_s t_2) - (L_s - D_3 - L_s f_s t_2)sin(2\pi f_s t_1)}{[cos(2\pi f_s t_1) - 1]sin(2\pi f_s t_2) - [cos(2\pi f_s t_2) - 1]sin(2\pi f_s t_1)} \end{cases} \tag{12}$$

Figure 5 presents the longitudinal displacement, velocity, and acceleration of CoM trajectory at different step frequencies, with a fixed step length of 0.6 m. Over the interval from $t = 0$ to $t = T_s$, CoM displacement consistently increases from 0 to L_s, while the velocity and acceleration at the two endpoints $t = 0$ and $t = T_s$ remain equal, thus satisfying the periodic boundary conditions required for continuous gait cycles.

It is evident that step frequency has only a marginal effect on the displacement amplitude (**Figure 5a**), but considerably affects both velocity and acceleration. In particular, higher frequencies yield larger peak velocities: at 1.6 Hz, the velocities at the beginning and end of the step are approximately 1.3 m/s, whereas at 2.4 Hz they rise to about 1.8 m/s (**Figure 5b**). The same trend holds for acceleration: higher step frequencies push the amplitude upward (**Figure 5c**). The velocity–acceleration phase portraits in **Figure 5d** remain closed loops across the tested range, confirming the intrinsic stability of the reference trajectory. As step frequency increases, the loops change character, evolving from horizontally elongated ellipses toward roughly circular forms. This reshaping reflects the fact that acceleration outpaces velocity growth, and it suggests that inertial forces, rather than velocity-dependent effects, dominate the system's frequency sensitivity.

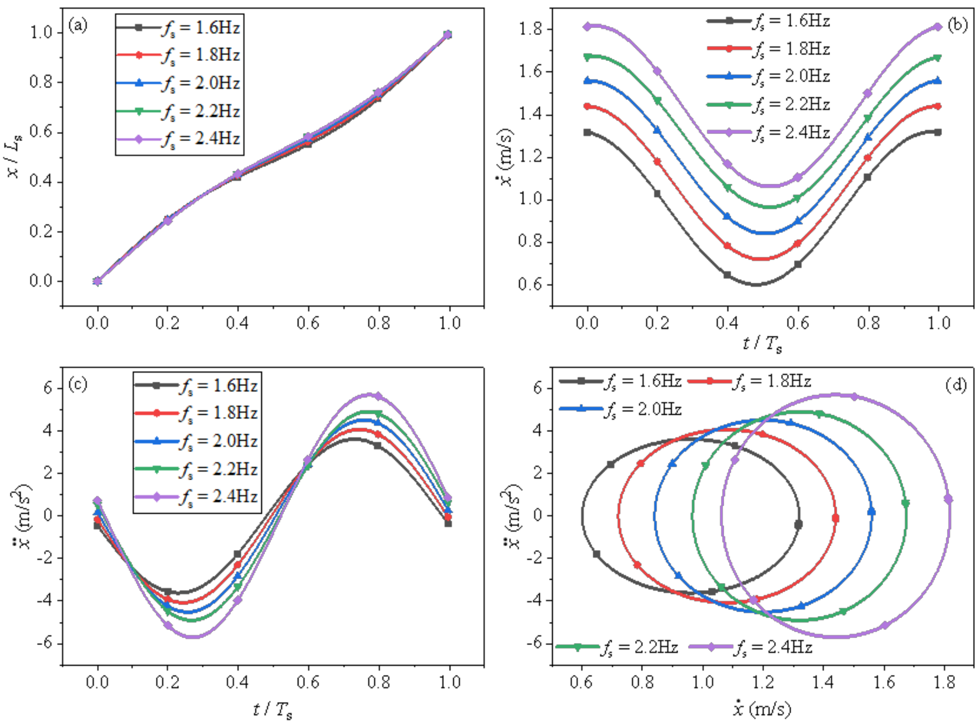

Figure 5. Longitudinal trajectory (L_s = 0.6 m).

In summary, the proposed longitudinal CoM reference trajectory fully satisfies the boundary conditions, is smooth throughout the step, and thus provides a reliable basis for planning bipedal longitudinal walking trajectories [32].

4. Vertical and lateral design of CoM trajectory

Now it proceeds to address the vertical and lateral swing trajectories of CoM. It follows that the vertical trajectory $z(t)$ should satisfy the same displacement, velocity, and acceleration at time 0 and time T_s. For $y(t)$, in addition to having equal velocity and acceleration at time 0 and T_s, it must also satisfy $y(0) = -y(T_s)$ [33]. Beyond the above conditions, it is also required that $z(t)$ and $y(t)$ satisfy the boundary conditions of the following equation at times t_1 and t_2.

$$\begin{cases} z^2\left(t_1\right)+\left[\frac{L_w}{2}-y\left(t_1\right)\right]^2+\left(L_s-D_1\right)^2=l_0^2 \\ z^2\left(t_2\right)+\left[\frac{L_w}{2}+y\left(t_2\right)\right]^2+\left(L_s-D_3\right)^2=l_0^2 \\ k_{\text{leg}}\left(\frac{l_o}{\sqrt{y^2(0)+z^2(0)}}-1\right)z(0)=F\left(T_v\right) \end{cases} \tag{13}$$

To satisfy the above boundary conditions, Fourier series are adopted for $y(t)$ and

$z(t)$. Given the constraints imposed by Equation (13) above, the total number of Fourier coefficients for $y(t)$ and $z(t)$ is three. Based on this number of coefficients and the temporal boundary conditions, the Fourier series expressions are assumed as $y(t)$ and $z(t)$ as follows:

$$\begin{cases} y(t) = A_y\left[9cos\left(\pi f_s t\right) - \cos\left(3\pi f_s t\right)\right] \\ z(t) = Z_0 + A_z cos\left(2\pi f_s t\right) \end{cases} \tag{14}$$

Substituting Equation (14) into Equation (13) yields the following strongly nonlinear equation:

$$\begin{cases} \left(Z_0 + A_z c_1\right)^2 + \left(\frac{L_w}{2} - \left|A_y c_3\right|\right)^2 + \left(L_s - D_1\right)^2 = l_0^2 \\ \left(Z_0 + A_z c_2\right)^2 + \left(\frac{L_w}{2} - \left|A_y c_4\right|\right)^2 + \left(L_s - D_3\right)^2 = l_0^2 \\ \left[\frac{l_0}{\sqrt{64A_y^2 + \left(Z_0 + A_z\right)^2}} - 1\right]\left(Z_0 + A_z\right) = \delta_v \end{cases} \tag{15}$$

Where $\begin{cases} c_1 = cos\left(2\pi f_s t_1\right) \\ c_2 = cos\left(2\pi f_s t_2\right) \\ c_3 = 9cos\left(\pi f_s t_1\right) - cos\left(3\pi f_s t_1\right) \\ c_4 = 9cos\left(\pi f_s t_2\right) - cos\left(3\pi f_s t_2\right) \\ \delta_v = \dfrac{F\left(T_v\right)}{k_{\text{leg}}} \end{cases}$

It is worth noting that, the lateral displacement $y(t)$ describes the side-to-side sway of the center of mass about the central line; adopting the convention that $y(t_1)$ is positive at the initial instant, the center of mass sways to the opposite side at the subsequent critical instant t_2. As a result, the relative positions of the center of mass and the supporting foot at these two instants are geometrically inverted, and the corresponding lateral clearance must therefore be expressed with opposite signs. The term $L_w/2 - |A_y c_4|$ appearing in Equation (15) correctly captures this reversal and ensures that the constraint fundamentally describes the same physical requirement as in Equation (13)—namely, that the y-direction distance from the center of mass to the inner edge of the supporting foot remains within the allowable half of step width L_w.

The equation is strongly nonlinear and has no analytical solution. Here, a constrained parameter optimization approach is adopted to solve them. Define the variable vector $\boldsymbol{X} = [A_z, Z_0, A_y]^T$. The system of equations can be written as:

$$\boldsymbol{F}\left(\boldsymbol{X}\right) = \boldsymbol{0},\ \boldsymbol{F} = \left[f_1\left(\boldsymbol{X}\right) \quad f_2\left(\boldsymbol{X}\right) \quad f_3\left(\boldsymbol{X}\right)\right]^T \tag{16}$$

where $\begin{cases} f_1\left(\boldsymbol{X}\right) = \frac{1}{l_0^2}\left[\left(Z_0 + A_z c_1\right)^2 + \left(\frac{L_w}{2} - \left|A_y c_3\right|\right)^2 + \left(L_s - D_1\right)^2\right] - 1 \\ f_2\left(\boldsymbol{X}\right) = \frac{1}{l_0^2}\left[\left(Z_0 + A_z c_2\right)^2 + \left(\frac{L_w}{2} - \left|A_y c_4\right|\right)^2 + \left(L_s - D_3\right)^2\right] - 1 \\ f_3\left(\boldsymbol{X}\right) = \frac{1}{l_0^2}\left[\left(Z_0 + A_z + \delta_v\right)\sqrt{64A_y^2 + \left(Z_0 + A_z\right)^2}\right] - \frac{\left(Z_0 + A_z\right)}{l_0} \end{cases}$

Solving the system is equivalent to minimizing the sum of squared residuals:

$$\min_{\boldsymbol{X}} \hbar\left(\boldsymbol{X}\right) = \frac{1}{2}\sum\nolimits_{i=1}^{3} f_i\left(\boldsymbol{X}\right)^2 \tag{17}$$

Subject to the inequality constraints:

$$\begin{cases} 0 < Z_0 < l_0 \\ 0 < A_z \ < l_0 \\ Z_0 + A_z < l_0 \\ 0 < A_y \leq \frac{L_w}{16} \end{cases} \tag{18}$$

Construct a single layer linear constrained parameter optimization whose input is a fixed constant and whose outputs are the variables $\boldsymbol{X}$. The network architecture is:

Input layer: 1 node, always equal to 1.

Output layer: 3 nodes, no activation function. The output is $\boldsymbol{X} = w + b$, where w is a 3×1 weight matrix and b is a 3×1 bias vector. In practice, $\boldsymbol{X}$ is directly treated as the set of trainable parameters.

Training proceeds by minimizing the loss $\varepsilon(\boldsymbol{X})$ with gradient descent, while penalty terms are added to handle the constraints. A penalty function method is adopted. The constraints are incorporated into the loss by adding penalty terms:

$$\begin{aligned} \varepsilon_{\text{total}}(\boldsymbol{X}) = \frac{1}{2}\sum_{i=1}^{3} f_i(\boldsymbol{X})^2 + \lambda_1[max(0, -Z_0)]^2 + \lambda_2[max(0, Z_0 - l_0)]^2 \\ + \lambda_3[max(0, -A_z)]^2 + \lambda_4[max(0, Z_0 + A_z - l_0)]^2 \\ + \lambda_5[max(0, -A_y)]^2 + \lambda_6\left[max\left(0, A_y\frac{-L_w}{16}\right)\right]^2 \end{aligned} \tag{19}$$

where each $\lambda_i > 0$ is a penalty coefficient. Whenever a variable violates a constraint, the corresponding penalty term produces a large loss, driving the variables back into the feasible region.

The variable $\boldsymbol{X}$ is updated using the Adam optimizer (adaptive moment estimation) [34]. The iterative scheme is:

$$\boldsymbol{X}^{(n+1)} = \boldsymbol{X}^{(n)} - \eta \cdot \text{Adam}\left(\nabla_{\boldsymbol{x}}\varepsilon_{\text{total}}\left(\boldsymbol{X}^{(n)}\right)\right) \tag{20}$$

To obtain the parametric solution for the reference trajectory, the following pedestrian parameters are adopted as a numerical example: body mass m = 80 kg, leg stiffness k_{leg} = 20 kN/m, leg natural length l_0 = 1.0 m, and step width L_w = 0.1 m. The penalty coefficients λ_1 to λ_6 are set to 20, 10, 60, 50, 40, and 40, respectively; the Adam parameter η is set to 0.95; and the maximum number of iterations is set to 10,000. After calculation, it is found that the loss function converges well (**Figure 6**). Computational results indicate that the loss function converges rapidly to a steady value under all tested combinations of step frequency and step length. As the step frequency increases from 1.6 Hz to 2.4 Hz, the convergence rate accelerates consistently. For instance, in subplot **Figure 6a**, at 1.6 Hz, approximately 8,000 iterations are required to reach convergence, whereas at 2.4 Hz, the loss function essentially stabilizes within 4,000 iterations. A similar trend is observed in subplot **Figure 6b** for a step length of 0.7 m, where convergence is achieved after about 6,000 iterations at 1.6 Hz, but again reduces to roughly 4,000 iterations at 2.4 Hz. Comparing subplots **Figure 6a** and **Figure 6b**, it is evident that the convergence rate for a 0.7 m step length is consistently faster than that for 0.6 m across the tested frequency range. Furthermore, the convergence histories are notably smooth and free from oscillations or irregularities, indicating that the optimization process is numerically stable throughout.

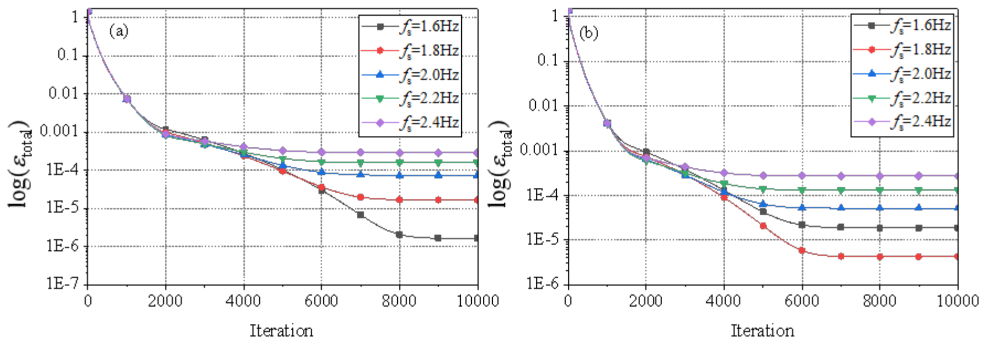

Figure 6. Loss function convergence curve with **(a)** L_s = 0.6 m and **(b)** L_s = 0.7 m.

Table 2 presents the numerical results of the center-of-mass trajectory parameters, with all values rounded to six decimal places. Under varying step frequencies and step lengths, the parameters Z_0, A_z, and A_y exhibit corresponding variations. Specifically, Z_0 ranges from 0.93 to 0.96, A_z falls between 0.02 and 0.04, and A_y lies approximately in the range of 0.002 m to 0.004 m.

Table 2. Parameter results of vertical and lateral trajectory.

	f_s (Hz)	1.6	1.8	2.0	2.2	2.4
L_s = 0.6 m	Z_0 (m)	0.945599	0.947426	0.949068	0.950643	0.951414
	A_z (m)	0.022974	0.02496	0.026588	0.028103	0.028952
	A_y (m)	0.002891	0.002860	0.002864	0.002878	0.002918
L_s = 0.7 m	Z_0 (m)	0.934115	0.936051	0.937738	0.939334	0.940131
	A_z (m)	0.033858	0.036082	0.037792	0.039338	0.040219
	A_y (m)	0.003006	0.002937	0.002925	0.002931	0.002967

Based on these parameters, **Figure 7** presents the trajectories of displacement, velocity, and acceleration of the CoM in the vertical and lateral directions over a single step cycle with a 0.6 m step length. **Figure 7a–c** present the lateral displacement, velocity, and acceleration trajectories of CoM, respectively. Step frequency exerts a negligible influence on the lateral displacement oscillation, whereas both the velocity and acceleration amplitudes increase with higher step frequencies. This indicates that an elevated step frequency markedly alters the lateral velocity and acceleration of CoM, thereby intensifying the challenge of maintaining stability. **Figure 7d–f** display the vertical displacement, velocity, and acceleration reference trajectories of CoM. As step frequency increases, the maximum vertical displacement rises from approximately 0.97 m to 0.98 m, while the minimum value remains nearly unchanged, suggesting that variations in step frequency primarily affect the peak vertical displacement of the bipedal CoM. When the step frequency exceeds 2.4 Hz, the maximum vertical displacement further increases until the feet lose contact with the ground and the gait transitions to running. The vertical velocity and acceleration amplitudes also increase significantly with step frequency, consistent with the pattern observed in the lateral direction. Consequently, higher step frequencies are accompanied by larger CoM oscillation amplitudes and heightened postural instability.

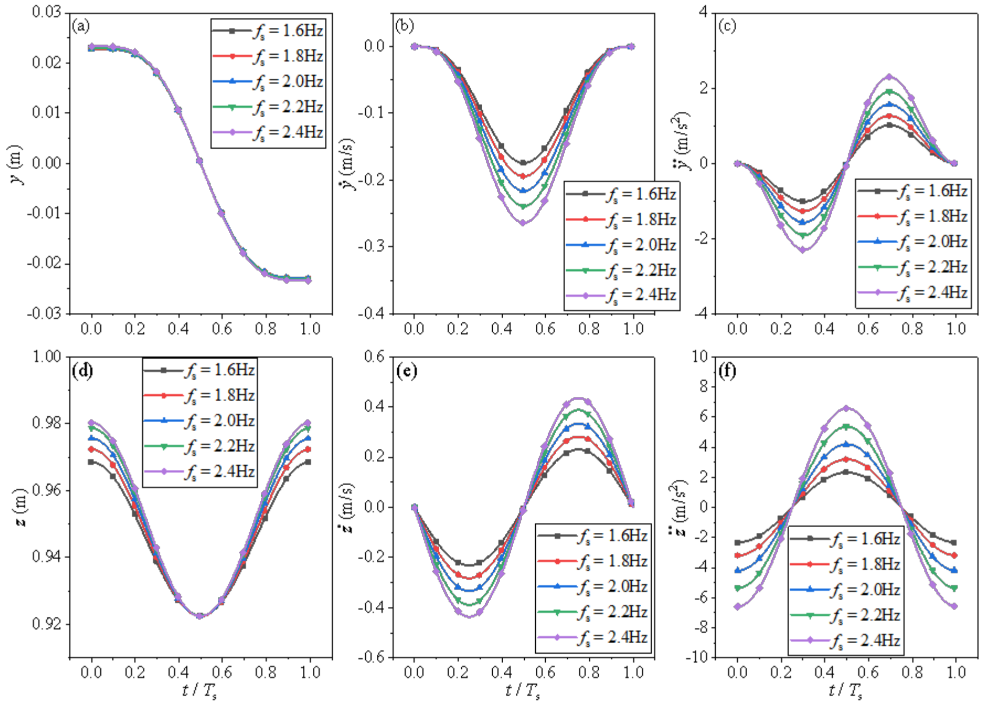

Figure 7. Trajectory response under single-step duration with L_s = 0.6 m.

Figure 8 presents the reconstructed ground reaction force (GRF) profiles based on reference trajectories for step lengths of 0.6 m and 0.7 m, respectively. In both panels, the curves marked with black filled circles denote the GRFs derived from the trajectory-referenced (TR) method, whereas the curves marked with open circles represent the GRFs obtained using the dynamic load factor (DLF) approach. Despite discrepancies in amplitude between the GRFs constructed via the TR method and those based on the DLF method, the TR-based GRFs successfully capture the fundamental characteristics of the pedestrian foot–ground reaction force, including the double-peak convex pattern during the stance phase and the concave valley in the mid-stance region. Overall, the discrepancy between the two methods increases with step length. Since the reference trajectories used in the TR method do not account for the contribution of damping, the TR-based GRFs are generally smaller than those derived from the DLF method.

The relative error (**Figure 9**) between the two approaches is quantified as the difference between the TR-based GRF and the DLF-based GRF divided by the DLF-based GRF. The results indicate that the relative error for the 0.6 m step length is generally larger than that for the 0.7 m step length. However, as step frequency increases, the rate of increase in relative error diminishes, reaching a maximum at approximately 2.2 Hz, where the peak relative error is around 22%. These findings suggest that the current method is not yet fully refined and still warrants further improvement. Nevertheless, as a reference trajectory, it adequately reproduces the essential characteristics of pedestrian gait and can serve as a valid reference.

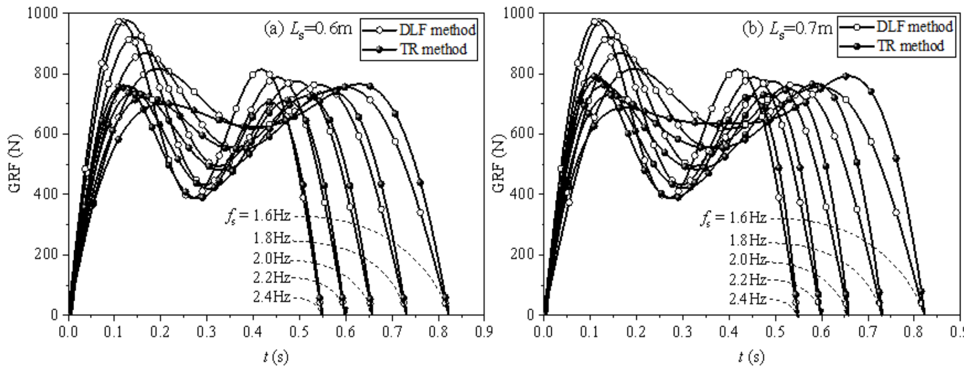

Figure 8. GRF reconstruction for DLF and Trajectory Reference (TR) with **(a)** L_s = 0.6 m and **(b)** L_s = 0.7 m.

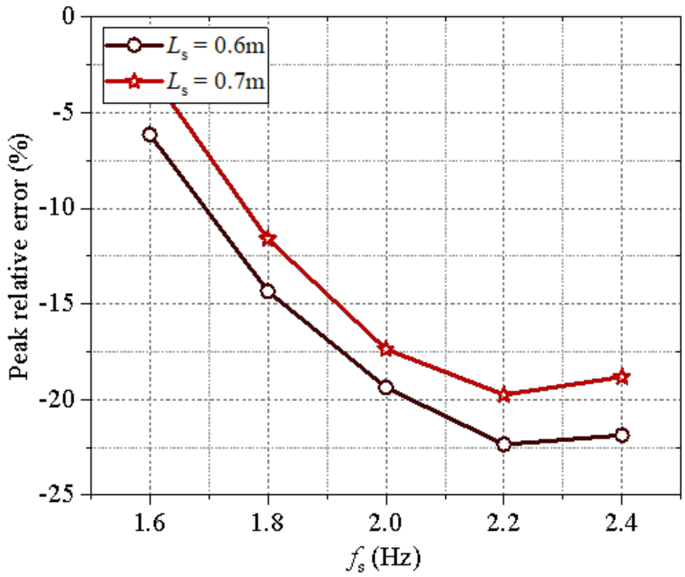

Figure 9. Relative peak error of GRF reconstruction based on trajectory reference.

5. Application validation

To see whether the CoM trajectory algorithm holds up in an engineering setting, we applied it to the bipedal walking model shown in **Figure 10**.

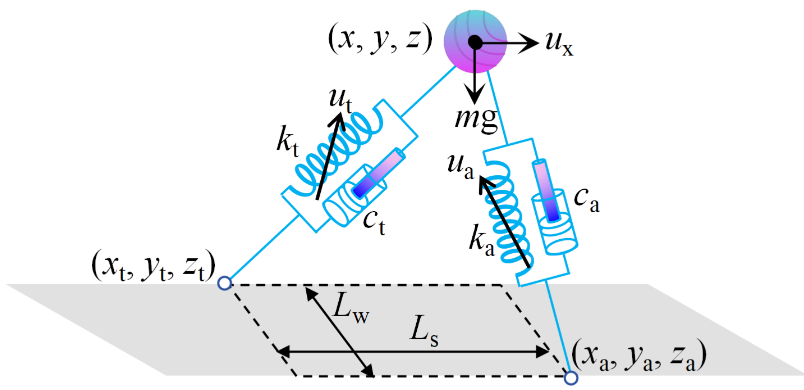

Figure 10. Bipedal walking mode.

In this setup, the CoM is located by coordinates (x, y, z), and the advancing leg is assigned stiffness k_a, damping c_a, and a control force u_a. Similarly, the trailing leg possesses leg stiffness (k_t), damping (c_t), and a control force (u_t). The stiffness and damping of the bipedal leg are related to the leg length distribution, and the specific expressions are given in Gao et al. [35, 36]. The coordinates of the leading foot and trailing foot touching points are (x_a, y_a, z_a) and (x_t, y_t, z_t), respectively. L_s and L_w represent the step length and step width. Under the assumptions of no leg crossing during walking and no slipping at the foot-ground contact points, the system's kinetic energy is given as follows:

$$\begin{cases} T = \frac{1}{2}m\left(\dot{x}^2 + \dot{y}^2 + \dot{z}^2\right) \\ V = \frac{1}{2}k_a\left(l_0 - l_a\right)^2 + \frac{1}{2}k_t\left(l_0 - l_t\right)^2 + u_a\left(l_0 - l_a\right) + u_t\left(l_0 - l_t\right) + mgz \end{cases} \tag{21}$$

Here, l_0, l_a, and l_t are the natural leg length, the leading leg length, and the trailing leg length, respectively, where l_a and l_t can be calculated from the geometric relationship between the center-of-mass coordinates and the pedestrian's foot coordinates.

After substituting Equation (21) into the Lagrange equation, the system dynamic equation can be obtained as Equation (22).

$$\boldsymbol{M}\ddot{\boldsymbol{q}} + \boldsymbol{C}\dot{\boldsymbol{q}} + \boldsymbol{K}\boldsymbol{q} = \boldsymbol{F} + \boldsymbol{B}\boldsymbol{u} \tag{22}$$

where $\boldsymbol{M}$ = diag $\begin{pmatrix} m & m & m \end{pmatrix}$, $\boldsymbol{K}$ = diag $\begin{pmatrix} k_\Delta & k_\Delta & k_\Delta \end{pmatrix}$, $\boldsymbol{q} = \begin{bmatrix} x & y & z \end{bmatrix}^T$ and $\boldsymbol{u} = \begin{bmatrix} u_a & u_t & u_x \end{bmatrix}^T$ are the absolute force vectors induced by the structural floor vibration; u_x is the control torque that drives the pedestrian forward; $\boldsymbol{C}$, $\boldsymbol{B}$ and $\boldsymbol{F}$ are the damping matrix, the control configuration matrix and the force vector, respectively, and their expressions are:

$$\boldsymbol{C} = \begin{bmatrix} c_{xx} & c_{xy} & c_{xz} \\ c_{xy} & c_{yy} & c_{yz} \\ c_{xz} & c_{yz} & c_{zz} \end{bmatrix}, \boldsymbol{B} = \begin{bmatrix} \frac{x_{l_a}}{l_a} & \frac{x_{l_t}}{l_t} & \frac{1}{z-z_0} \\ \frac{y_{l_a}}{l_a} & \frac{y_{l_t}}{l_t} & 0 \\ \frac{z_{l_a}}{l_a} & \frac{z_{l_t}}{l_t} & 0 \end{bmatrix}, \boldsymbol{F} = \begin{bmatrix} k_{\Delta a}x_a + k_{\Delta t}x_t \\ k_{\Delta a}y_a + k_{\Delta t}y_t \\ k_{\Delta a}z_a + k_{\Delta t}z_t - mg \end{bmatrix}$$

In the above equations, $c_{\sigma\tau}$ represents the projected components of leg damping in spatial directions, expressed in tensor form as: $c_{\sigma\tau} = \sum_{\chi=\mathrm{a,t}} c_{\chi\sigma\tau}$, $c_{\chi\sigma\tau} = c_\chi\left(\frac{\sigma_{l_\chi}\tau_{l_\chi}}{l_\chi^2}\right)$, $(\chi = a, t;\ \sigma, \tau = x, y, z)$.$k_\Delta = k_{\Delta a} + k_{\Delta t}$,$k_{\Delta a} = k_a\left(1 - \frac{l_0}{l_a}\right)$, $k_{\Delta t} = k_t\left(1 - \frac{l_0}{l_t}\right)$ are the stiffness coefficients of the pedestrian's advancing leg and trailing leg, respectively; z_0 is the vertical coordinate of the ground. During single-leg support, this value is taken as the vertical coordinate of the supporting foot sole; during double-leg support, it is taken as the average value of the vertical coordinates of both foot soles.

5.1. System state control equation

The dynamic Equation (22) of a bipedal walking can be transformed into the standard nonlinear state-space control equations as follows:

$$\frac{dq}{dt} = f(q) + g(q)u \tag{23}$$

where the variable column vectors are:

$$q = \begin{bmatrix} q_1 & q_2 & q_3 & q_4 & q_5 & q_6 \end{bmatrix}^T = \begin{bmatrix} x & y & z & \dot{x} & \dot{y} & \dot{z} \end{bmatrix}^T,$$

$$f(q) = \begin{bmatrix} q_4 \\ q_5 \\ q_6 \\ -\frac{1}{m}\left(k_\Delta q_1 + c_{xx} q_4 + c_{xy} q_5 + c_{zx} q_6\right) + \frac{1}{m}\left(k_{\Delta a} x_a + k_{\Delta t} x_t\right) \\ -\frac{1}{m}\left(k_\Delta q_2 + c_{xy} q_4 + c_{yy} q_5 + c_{yz} q_6\right) + \frac{1}{m}\left(k_{\Delta a} y_a + k_{\Delta t} y_t\right) \\ -\frac{1}{m}\left(k_\Delta q_3 + c_{zx} q_4 + c_{yz} q_5 + c_{zz} q_6\right) + \frac{1}{m}\left(k_{\Delta a} z_a + k_{\Delta t} z_t\right) - g \end{bmatrix},$$

$$g(q) = \begin{bmatrix} 0 & 0 & 0 \\ 0 & 0 & 0 \\ 0 & 0 & 0 \\ \frac{q_1 - x_a}{m l_a} & \frac{q_1 - x_t}{m l_t} & \frac{1}{m(q_3 - z_0)} \\ \frac{q_2 - y_a}{m l_a} & \frac{q_2 - y_t}{m l_t} & 0 \\ \frac{q_3 - z_a}{m l_a} & \frac{q_3 - z_t}{m l_t} & 0 \end{bmatrix},$$

and control column vector is $u = \begin{bmatrix} u_a & u_t & u_x \end{bmatrix}^T$.

5.2. Stability control strategy

The control for forward speed, lateral sway, and height is to make CoM track a desired trajectory, and the tracking sliding surfaces are defined as follows:

$$s = \begin{bmatrix} s_x \\ s_y \\ s_z \end{bmatrix} = \begin{bmatrix} q_1 - x_{\text{ref}} \\ \left(q_5 - \dot{y}_{\text{ref}}\right) + \lambda_y \left(q_2 - y_{\text{ref}}\right) \\ \left(q_6 - \dot{z}_{\text{ref}}\right) + \lambda_z \left(q_3 - z_{\text{ref}}\right) \end{bmatrix} \tag{24}$$

where s_x, s_y, and s_z represent the sliding surfaces for forward velocity, lateral swing displacement, and vertical height, respectively, and λ_y and λ_z are the associated coefficients controlling the convergence rate. Differentiating the three sliding surface functions gives their derivatives in matrix form as follows:

$$\dot{s} = \begin{bmatrix} \dot{q}_1 - \dot{x}_{\text{ref}} \\ \left(\dot{q}_5 - \ddot{y}_{\text{ref}}\right) + \lambda_y \left(q_5 - \dot{y}_{\text{ref}}\right) \\ \left(\ddot{q}_6 - \ddot{z}_{\text{ref}}\right) + \lambda_z \left(q_6 - \dot{z}_{\text{ref}}\right) \end{bmatrix} = \Gamma + J(q)u - R = -\kappa sign(s) \tag{25}$$

Where $J(q) = \frac{1}{m}\begin{bmatrix} \frac{q_1 - x_a}{l_a} & \frac{q_1 - x_t}{l_t} & \frac{1}{(q_3 - z_0)} \\ \frac{q_2 - y_a}{l_a} & \frac{q_2 - y_t}{l_t} & 0 \\ \frac{q_3 - z_a}{l_a} & \frac{q_3 - z_t}{l_t} & 0 \end{bmatrix}$, $R = \begin{bmatrix} \dot{x}_{\text{ref}} \\ \ddot{y}_{\text{ref}} \\ \ddot{z}_{\text{ref}} \end{bmatrix}$, $\kappa = \begin{bmatrix} \kappa_x & 0 & 0 \\ 0 & \kappa_y & 0 \\ 0 & 0 & \kappa_z \end{bmatrix}$

$$\Gamma(q) = \begin{bmatrix} -\frac{k_\Delta q_1 + c_{xx} q_4 + c_{xy} q_5 + c_{zx} q_6}{m} + \frac{k_{\Delta a} x_a + k_{\Delta t} x_t}{m} \\ -\frac{k_\Delta q_2 + c_{xy} q_4 + c_{yy} q_5 + c_{yz} q_6}{m} + \frac{k_{\Delta a} y_a + k_{\Delta t} y_t}{m} + \lambda_y \left(q_5 - \dot{y}_{\text{ref}}\right) \\ -\frac{k_\Delta q_3 + c_{zx} q_4 + c_{yz} q_5 + c_{zz} q_6}{m} + \frac{k_{\Delta a} z_a + k_{\Delta t} z_t}{m} - g + \lambda_z \left(q_6 - \dot{z}_{\text{ref}}\right) \end{bmatrix}$$

The final control law is derived from Equation (25) and given as Equation (26):

$$u = u_{\text{eq}} + u_{\text{sw}} = J(q)^{-1}\left[R - \Gamma(q) - \kappa sign(s)\right] \tag{26}$$

To verify the applicability of the reference trajectory and the sliding mode control theory for bipedal walking, a simulation is conducted using the following parameters: body mass m = 80 kg, leg damping ratio ξ_{leg} = 8%, leg stiffness k_{leg} = 20 kN/m, leg natural length l_0 = 1.0 m, and step width L_w = 0.1 m. The control parameters λ_y, and λ_z are set to 3, and 5, respectively, while κ_x, κ_y, and κ_z are set to 20, 20, and 20, respectively. Simulation results demonstrate that the proposed approach is capable of generating satisfactory reference trajectories. **Figure 11** illustrates CoM response during bipedal walking based on the GRF reference trajectory developed in this study. **Figure 11a,d,g** present the displacement, velocity, and acceleration responses of CoM in the x-direction, respectively, where "REF" denotes the reference trajectory, and "SMC" and "LIP" refer to the sliding mode control method proposed in this paper and the linear inverted pendulum method, respectively. As shown, the SMC-based response trajectories closely track the reference trajectory, whereas the LIP method loses stability after approximately 2 s. **Figure 11b,e,h** depict the lateral displacement, velocity, and acceleration responses of CoM. The SMC method effectively follows the reference trajectory, while the LIP method exhibits drift instability, deviating from the reference trajectory within a few seconds. Similarly, **Figure 11c,f,i** show that the SMC method maintains stable walking, whereas the vertical response under the LIP method loses stability after approximately 1.5 s. These results indicate that the proposed method provides effective reference trajectories for bipedal walking, and the SMC method achieves stable control, demonstrating a successful integration of the two approaches.

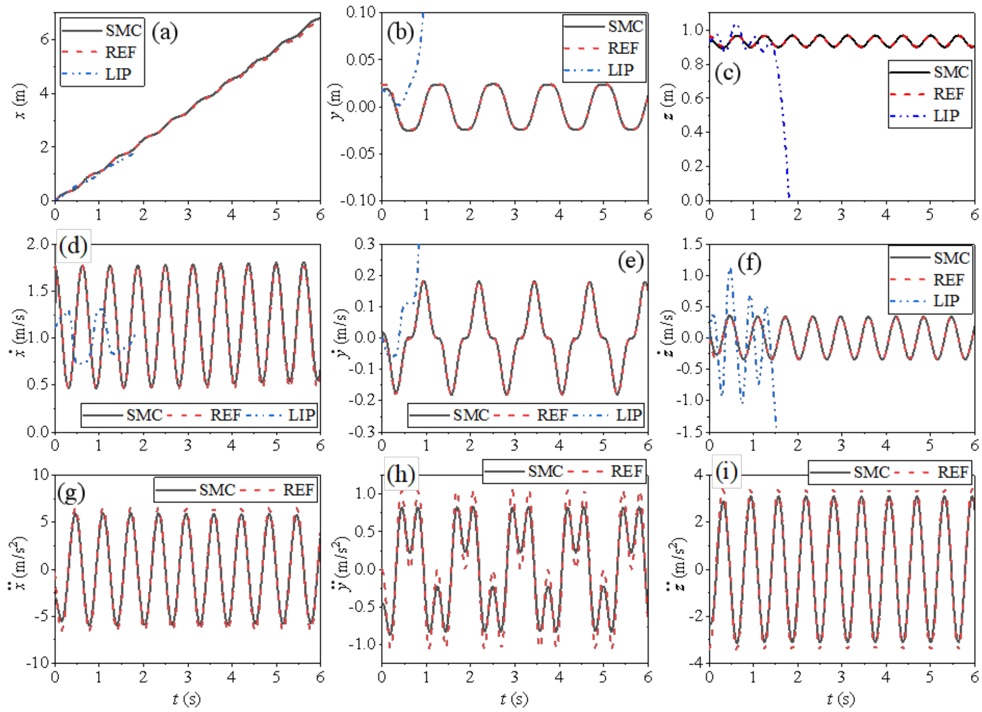

Figure 11. Bipedal CoM response at a 1.6 Hz walking step.

Figure 12 presents the Fast Fourier Transform (FFT) spectra of the mass acceleration responses in the longitudinal (**Figure 12a**), lateral (**Figure 12b**), and vertical (**Figure 12c**) directions, respectively. As shown, the spectral peaks of the longitudinal (**Figure 12a**) and vertical (**Figure 12c**) responses both occur at 1.6 Hz. In contrast, the lateral response spectrum (**Figure 12b**) exhibits peaks on either side of 1.6 Hz, specifically at 0.75 Hz and 2.3 Hz. This deviation arises because the lateral acceleration profile during bipedal walking differs markedly from those in the longitudinal and vertical directions, displaying a distinct double-peak characteristic. Consequently, the dominant frequency of the lateral response does not coincide with the step frequency, and both the lateral response and its control merit particular attention.

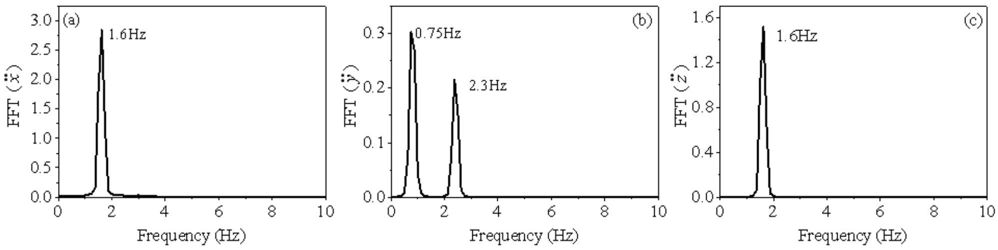

Figure 12. Fast Fourier Transform of CoM acceleration.

An analysis of the sliding mode control parameters reveals that no set of parameter values enables the bipedal walker to maintain stable walking indefinitely; stability is invariably lost after a finite number of steps. The authors have conducted extensive investigations into this phenomenon but have not yet arrived at a theoretical explanation. Nevertheless, the influence ranges of the parameters have been identified through simulation-based analysis. **Figure 13** presents contour plots of the number of stable walking steps achieved under different combinations of κ_x , κ_y, and κ_z. For instance, **Figure 13a** shows that when κ_z is fixed at 60, varying κ_x and κ_y yields a maximum of 20 stable steps. **Figure 13b** indicates that with κ_x fixed at 20, the maximum number of stable steps reaches 33 as κ_y and κ_z vary. **Figure 13c** demonstrates that when κ_y is fixed at 20, the maximum number of stable steps is 25 under variations in κ_x and κ_z. These examples illustrate the number of stable walking steps when two parameters are varied while the others are held constant. In practice, given the large number of parameters involved in sliding mode control, a systematic analysis of their effects on the number of stable bipedal steps constitutes an exceedingly complex and time-consuming endeavor that cannot be accomplished through exhaustive comparative analysis alone. Prior to a theoretical breakthrough, the numerical analysis over a selected range of parameter values can only serve as a reference. A definitive determination of the stability parameter ranges will require further theoretical advances.

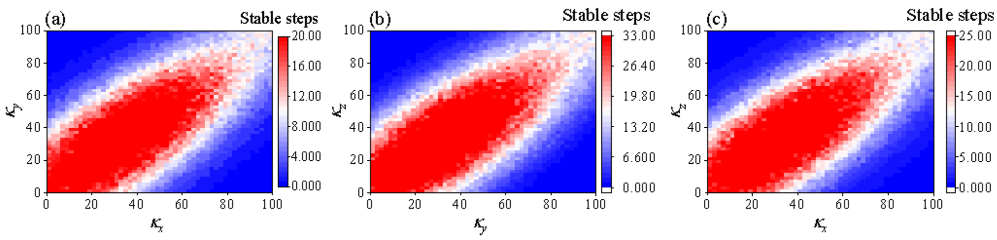

Figure 13. Stable region for sliding mode control parameters.

In establishing the reference trajectory, the contribution of leg damping was deliberately excluded. This is because the damping force of the human leg is velocity-dependent, and incorporating it would introduce additional parameters, rendering the governing equations overly complex and intractable. By omitting damping, the GRF-based reference trajectory model retains a simpler formulation with fewer parameters, yet remains capable of accurately capturing the essential characteristics of bipedal walking.

In the subsequent application of sliding mode control (SMC) for bipedal walking, however, leg damping was explicitly incorporated. This is justified by the fact that energy is continuously dissipated during human walking. If control inputs were applied without accounting for energy dissipation through damping, the system energy would accumulate progressively, leading to a response that fails to reflect realistic control effects. Moreover, the theoretical frameworks differ between the two stages: the SMC-based bipedal control adopts a control-theoretic approach, whereas the earlier GRF-based reference trajectory was derived from force equilibrium and displacement compatibility. Consequently, the omission of damping in the reference trajectory construction does not undermine the validity of the SMC-based bipedal walking control.

Any discrepancy that does arise stems from the difference between the damped and undamped GRF trajectories. In practice, the leg damping force is considerably smaller than the leg stiffness force, so the resulting GRF trajectory remains a suitable reference for bipedal walking applications. Simulation results further confirm that the proposed reference trajectory can effectively serve as a reference for SMC-based bipedal walking control [37].

6. Conclusion

This study presented a method for generating CoM reference trajectories directly from ground reaction force dynamics, without relying on iterative integration or online optimization. By embedding the GRF profile into a unified spatio-temporal framework and solving for the trajectory coefficients through constrained residual minimization, the approach produces smooth, physically consistent CoM paths that naturally capture the double-peak loading characteristic of bipedal walking. The resulting Fourier-based representation is compact, computationally inexpensive, and accurately reflects how step frequency and step length shape the CoM motion in all three directions.

Simulation results show that step frequency has a weak influence on lateral displacement but markedly amplifies velocity and acceleration amplitudes in both the lateral and vertical directions, making stability harder to maintain at higher frequencies. The reconstructed GRFs from the proposed trajectories match the main features of the DLF-based profiles, with relative errors generally staying within an acceptable range. When integrated with sliding mode control, the reference trajectories enable stable bipedal walking over multiple steps. The SMC-controlled walker tracks the reference closely in the longitudinal, lateral, and vertical directions, whereas the conventional LIP-based method loses stability within a few seconds. Control parameter analysis reveals that no fixed parameter set guarantees indefinite stable walking, and the stable step count varies considerably across the parameter space, highlighting the need for further theoretical work.

The main limitation of the current framework is the exclusion of leg damping during trajectory construction, which leads to a systematic underestimation of the GRF amplitude. This gap is partially compensated in the SMC stage, but a more integrated treatment remains a direction for future work. Overall, the proposed method offers a practical and physically interpretable way to plan bipedal walking references and works effectively in combination with sliding mode control.

Author contributions: Conceptualization, YG and QZ; methodology, QZ and AH; software, AH and JG; validation, QZ, AH and SL; formal analysis, QZ and AH; investigation, QZ and EG; resources, YG and SL; data curation, QZ and QC; writing—original draft preparation, QZ and AH; writing—review and editing, YG, YC (Yanxiang Chen), YC (Yuanyang Chen) and YW; supervision, YG and SL; project administration, YG; funding acquisition, YG and YC (Yanxiang Chen). All authors have read and agreed to the published version of the manuscript.

Funding: The research is supported by the National Natural Science Foundation of China (Grant No. 51808247) and Hunan Provincial Natural Science Foundation of China (Grant No. 2024JJ6227).

Institutional review board statement: Not applicable.

Informed consent statement: Not applicable.

Data availability statement: The data used in this study are available from the corresponding author upon reasonable request.

Conflict of interest: The authors declare no conflict of interest.

AI use statement: During the preparation of this manuscript, the authors used DeepSeek solely for language refinement. No AI tools were used for data analysis, interpretation, or generation of scientific content. All outputs were critically reviewed and edited by the authors. The authors take full responsibility for the integrity and accuracy of the work.

References

1. Tesio L, Rota V. The motion of body center of mass during walking: A review oriented to clinical applications. Frontiers in Neurology. 2019; 10: 999. doi: 10.3389/fneur.2019.00999
2. Blickhan R. The spring-mass model for running and hopping. Journal of Biomechanics. 1989; 22(11–12): 1217–1227. doi: 10.1016/0021-9290(89)90224-8
3. Gao M, Xu Y, Zheng J, et al. Dynamic modeling and control of monopod 3D jumping robot. Light Industry Machinery. 2023; 41(5): 22–28. doi: 10.3969/j.issn.1005-2895.2023.05.004 (in Chinese)
4. Kajita S, Kanehiro F, Kaneko K, et al. Biped walking pattern generation by using preview control of zero-moment point. In: Proceedings of the 2003 IEEE International Conference on Robotics and Automation; 14–19 September 2003; Taipei, Taiwan. pp. 1620–1626. doi: 10.1109/ROBOT.2003.1241826
5. Yang H, Wu B, Li J, et al. A spring-loaded inverted pendulum model for analysis of human-structure interaction on vibrating surfaces. Journal of Sound and Vibration. 2022; 522: 116727. doi: 10.1016/j.jsv.2021.116727
6. Pratt JE, Tedrake R. Velocity-based stability margins for fast bipedal walking. In: Diehl M, Mombaur K (editors).

Fast Motions in Biomechanics and Robotics: Optimization and Feedback Control. Springer; 2006. Volume 340, pp. 299–324. doi: 10.1007/978-3-540-36119-0_14

7. Griffin TM, Main RP, Farley CT. Biomechanics of quadrupedal walking: How do four-legged animals achieve inverted pendulum-like movements? Journal of Experimental Biology. 2004; 207(20): 3545–3558. doi: 10.1242/jeb.01177
8. Siravuru A, Viswanathan SP, Sreenath K, et al. The reaction mass biped: Geometric mechanics and control. Journal of Intelligent & Robotic Systems. 2018; 89(1–2): 155–173. doi: 10.1007/s10846-017-0508-7
9. Geyer H, Herr H. A muscle-reflex model that encodes principles of legged mechanics produces human walking dynamics and muscle activities. IEEE Transactions on Neural Systems and Rehabilitation Engineering. 2010; 18(3): 263–273. doi: 10.1109/TNSRE.2010.2047592
10. Tang M, Zhang Y, Yu S, et al. Trajectory tracking model predictive control for mobile robot based on deep Koopman operator modeling. Robotics and Autonomous Systems. 2025; 194: 105152. doi: 10.1016/j.robot.2025.105152
11. Di Carlo J, Wensing PM, Katz B, et al. Dynamic locomotion in the MIT Cheetah 3 through convex model-predictive control. In: Proceedings of the 2018 IEEE/RSJ International Conference on Intelligent Robots and Systems; 1–5 October 2018; Madrid, Spain. pp. 1–9. doi: 10.1109/IROS.2018.8594448
12. Kim SH, Hong YD. Dynamic bipedal walking using real-time optimization of center of mass motion and capture point-based stability controller. Journal of Intelligent & Robotic Systems. 2021; 103(4): 58. doi: 10.1007/s10846-021-01468-1
13. Jeong H, Park S. Estimation of the ground reaction forces from a single video camera based on the spring-like center of mass dynamics of human walking. Journal of Biomechanics. 2020; 113: 110074. doi: 10.1016/j.jbiomech.2020.110074
14. Liang H, Zhang Z, Wei P. Theoretical derivation and parameters analysis of a human-structure interaction system with the bipedal walking model. Journal of Mathematics. 2021; 2021(1): 6683083. doi: 10.1155/2021/6683083
15. Ghaffarzadeh P, Chakraborty D, Aslansefat K, et al. A multi-modal dataset for ground reaction force estimation using consumer wearable sensors. Scientific Data. 2026; 13(1): 855. doi: 10.1038/s41597-026-07183-6
16. Gao Y, Yang Q. A walking crowd-structure interaction model. Journal of Vibration and Shock. 2016; 35(23): 153–159. doi: 10.13465/j.cnki.jvs.2016.23.024 (in Chinese)
17. Kuindersma S, Permenter F, Tedrake R. An efficiently solvable quadratic program for stabilizing dynamic locomotion. In: Proceedings of the 2014 IEEE International Conference on Robotics and Automation; 31 May–7 June 2014; Hong Kong, China. pp. 2589–2594. doi: 10.1109/ICRA.2014.6907230
18. Li Z, Huang R, Xiao F, et al. A centroidal dynamics-based MPC framework for agile bipedal walking. In: Proceedings of the 2025 IEEE 26th China Conference on System Simulation Technology and Its Applications; 11–13 July 2025; Shenzhen, China. pp. 291–296. doi: 10.1109/IEEECONF65522.2025.11137069
19. Vielemeyer J, Müller R, Staufenberg NS, et al. Ground reaction forces intersect above the center of mass in single support, but not in double support of human walking. Journal of Biomechanics. 2021; 120: 110387. doi: 10.1016/j.jbiomech.2021.110387
20. He Y, Wu M, Xia Y, et al. A novel and application-oriented inverse nodal problem for Sturm–Liouville operators. Mathematische Annalen. 2025; 393(3–4): 3119–3140. doi: 10.1007/s00208-025-03298-0
21. Hwangbo J, Lee J, Dosovitskiy A, et al. Learning agile and dynamic motor skills for legged robots. Science Robotics. 2019; 4(26): eaau5872. doi: 10.1126/scirobotics.aau5872
22. Bao L, Humphreys J, Peng T, et al. Deep reinforcement learning for robotic bipedal locomotion: A brief survey. Artificial Intelligence Review. 2026; 59(1): 38. doi: 10.1007/s10462-025-11451-z
23. Iida F, Rummel J, Seyfarth A. Bipedal walking and running with spring-like biarticular muscles. Journal of Biomechanics. 2008; 41(3): 656–667. doi: 10.1016/j.jbiomech.2007.09.033
24. Glackin C, Salge C, Greaves M, et al. Gait trajectory prediction using Gaussian process ensembles. In: Proceedings of the 2014 IEEE-RAS International Conference on Humanoid Robots; 18–20 November 2014; Madrid, Spain. pp. 628–633. doi: 10.1109/HUMANOIDS.2014.7041428
25. Huang F, Chen X, Liu Z, et al. Dynamic terrain gait control of biped robots based on environmental perception and reinforcement learning. In: Proceedings of the 7th International Conference on Artificial Intelligence and Advanced Manufacturing; 31 October–2 November 2025; Heidelberg, Germany. pp. 1048–1056. doi: 10.1049/icp.2025.4624
26. Yang QS, Qin JW, Law SS. A three-dimensional human walking model. Journal of Sound and Vibration. 2015; 357: 437–456. doi: 10.1016/j.jsv.2015.07.017
27. Fan JS, Chen Y, Nie JG. Modeling and validation of pedestrian-induced walking load on footbridges. Chinese Journal

of Computational Mechanics. 2012; 29(4): 538–544. (in Chinese)

28. Su T, Zhang H, Wang Y, et al. Dynamic picking algorithm based on Ferrari's method for Delta robot. Journal of Huazhong University of Science and Technology (Natural Science Edition). 2018; 46(6): 128–132. doi: 10.13245/j.hust.180623 (in Chinese)
29. Luo A, Li D, Wang S, et al. Perceptive locomotion and navigation for quadruped robots via depth-based representation. IEEE Transactions on Automation Science and Engineering. 2026; 23: 8672–8684. doi: 10.1109/TASE.2026.3687076
30. Cun C, Wu X, Xia H, et al. Decentralized repetitive learning for whole-body planning and control of humanoid robots with centroidal momentum dynamics. IEEE Transactions on Automation Science and Engineering. 2026; 23: 7932–7946. doi: 10.1109/TASE.2026.3679544
31. Gu Z, Li J, Shen W, et al. Humanoid locomotion and manipulation: Current progress and challenges in control, planning, and learning. IEEE/ASME Transactions on Mechatronics. 2026; 31(2): 2300–2330. doi: 10.1109/TMECH.2025.3579247
32. Yuan M, Yu T, Ge W, et al. A survey of behavior foundation model: Next-generation whole-body control system of humanoid robots. IEEE Transactions on Pattern Analysis and Machine Intelligence. 2026; 48(4): 4909–4927. doi: 10.1109/TPAMI.2025.3649177
33. Erlicher S, Trovato A, Argoul P. Modeling the lateral pedestrian force on a rigid floor by a self-sustained oscillator. Mechanical Systems and Signal Processing. 2010; 24(5): 1579–1604. doi: 10.1016/j.ymssp.2009.11.006
34. Shi Y, Yu B, Ba K, et al. A unified trajectory optimization approach for long-term and reactive motion planning of legged locomotion. Journal of Bionic Engineering. 2023; 20(5): 2108–2122. doi: 10.1007/s42235-023-00362-w
35. Gao YA, Yang QS, Dong Y, et al. Dynamic behavior of slab induced by pedestrian traffic. International Journal of Structural Stability and Dynamics. 2019; 19(12): 1950154. doi: 10.1142/S0219455419501542
36. Gao Y, Wang L, Yang Q, et al. Sliding mode control for stable bipedal locomotion: Reference trajectory design and stable analysis. International Journal of Applied Mechanics. 2026; 18(8): 2650064. doi: 10.1142/S175882512650064X
37. Sui JD, Chen WH, Shiang TY, et al. Real-time wearable gait phase segmentation for running and walking. In: Proceedings of the 2020 IEEE International Symposium on Circuits and Systems; 12–14 October 2020; Seville, Spain. pp. 1–5. doi: 10.1109/ISCAS45731.2020.9181210